31 Particle-Tracking Velocimetry

Dirk Engelmann, Michael Stöhr,
Christoph Garbe, and Frank Hering

Interdisziplinäres Zentrum für Wissenschaftliches Rechnen (IWR)
Universität Heidelberg, Germany

Handbook of Computer Vision and Applications
Volume 3
Systems and Applications

ISBN 0-12-379773-X/$30.00

31.1 Introduction

The need for quantitative flow field analysis has led to the development of various types of instruments. In most cases the measurement techniques were restricted to a single point in physical space, such as *laser doppler anemometry* (LDA. In recent years the rapid advances in computer technology enabled the extension of measuring techniques to two and three dimensions for standard applications.

Flow visualization techniques can be classified from different points of view. First, they can be distinguished by the method to make the flow visible. Either discrete particles or continuous tracers, such as fluorescent dyes using *laser induced fluorescence* (LIF), can be used to mark the flow field. Widely used in biological science (see Volume 1, Chapter 12), fluorescent tracers are also well-suited to observing mixing processes [1, 2, 3] and exchange processes. For an example, refer to *air-water gas exchange* in Chapter 30.

Second, we can differentiate flow visualization techniques by the type of velocity information that is obtained. Some techniques, such as *particle-imaging velocimetry* (PIV, for a review see Grant [4]) and least squares matching techniques [3] yield dense velocity fields. These techniques require, however, either a continuous fluorescent tracer or dense particles. With fluorescent tracers volumetric images must be taken so that only slow flows can be observed.

In contrast, *particle-tracking velocimetry* (PTV) does not yield dense velocity fields. The motion of individual particles is measured directly. In order to be able to track the particles, the particle concentrations must be much less than with PIV techniques. PIV techniques do not evaluate the velocity of individual particles, but correlate small regions between two images taken shortly in sequence.

For comparison of the different techniques it is important to note that Eulerian and Lagrangian flow fields are to be distinguished. *Eulerian flow field* measurements (see Adrian [5]) give the flow field as a function of space and time. This is the flow field that is obtained by PIV technqiues. Particle-tracking velocimetry provides—besides the Eulerian flow field— also the *Lagrangian* representation of the flow field. Each seeding particle is traced along its trajectory within the illluminated area. This path of an individual fluid element as a function of space and time is known as the Lagrangian flow field. The path $\boldsymbol{x}$ of a fluid element can be expressed as a function of the initial starting point $\boldsymbol{x}_0$ and of the elapsed time $t - t_0$

$$\boldsymbol{x} = \boldsymbol{x}(\boldsymbol{x}_0, t - t_0) \tag{31.1}$$

Its velocity $\boldsymbol{v}$ is given by

$$\boldsymbol{v} = \boldsymbol{v}(\boldsymbol{x}_0, t - t_0) = \frac{\partial \boldsymbol{x}}{\partial t}(\boldsymbol{x}_0, t - t_0) \tag{31.2}$$

Most PTV techniques use streak photography (see Hesselink [6]) as a tool for the determination of the flow field. The velocity field can be obtained by measuring length, orientation and location of each streak (see Gharib and Willert [7]). The length is commonly calculated from the end points of a streak, where the streaks are detected by a segmentation algorithm. This approach to PTV is only feasible at low particle concentrations of up to typically a few hundred particles/image (see Gharib and Willert [7], Adamczyk and Rimai [8]). Frequently used by many authors is a physical model which employs an interpolation scheme for identifying the same particle in the next image frame; see Section 31.4.

This chapter is restricted to PTV techniques because they yield both Eulerian and Lagrangian flow fields. They are also more suitable than PIV techniques with dense particle concentrations to be extended to true 3-D flow measurements. While standard PIV and PTV techniques give only a snapshot of the 2-D velocity field in a plane, we discuss in Section 31.3 the image processing techniques to track particles over long sequences of images. These techniques do not work with the standard thin laser illumination sheets because the particles leave this thin sheet too quickly to be tracked over an extended period of time. Thus we discuss several alternative illumination techniques in Section 31.2.

PTV techniques result in both Eulerian and Lagrangian flow fields and therefore allow to study the dynamics of the fluid flow. The flow fields still contain only a 2-D velocity restricted to a planar cross section involving one temporal and two spatial coordinates. In contrast, *stereoscopic PTV* (Section 31.4) yields 3-D flow fields in a volume, that is, the complete information of the physical space, which involves three spatial and one temporal coordinates.

31.2 Visualization

The visualization is part of the experimental setup. The aim of the visualization is to make the physical properties of a system optically visible. In the case of flow visualization either seeding particles or bubbles are placed in the fluid and illuminated by a light source with an optical lens system. The CCD camera then records the area of interest. In this way the seeding particles or bubbles represent the flow field of the liquid. An example of such a setup for particle-tracking velocimetry is shown in Fig. 31.4 and will be discussed more detailed in the next section.

The choice of the seeding particles has a major influence on the setup of the experiment. In Section 31.2.4 the properties of transparent seeding particles are discussed.

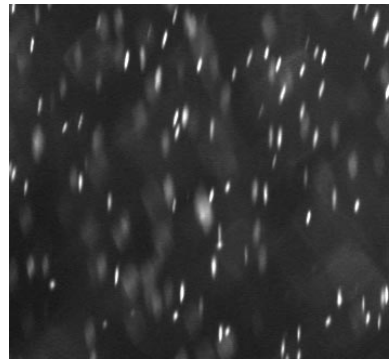

Figure 31.1: *Seeding particles in a light sheet illumination. Due to the exposure time of the camera particles in motion are visualized as streaks.*

31.2.1 Setup for particle-tracking velocimetry

The visualization in classical PTV uses a light sheet which cuts out a small slice of the fluid. The light sheet is typically generated by a laser scanner or by a bright light source with an optical system. For PTV a bright halogen lamp with a cylindrical lens and an aperture is of advantage. Due to the time of exposure of the CCD and the constant illumination, the seeding particles or bubbles are imaged as streak lines (see Fig. 31.1). The streak lines possess properties which are used in image sequence analysis (discussed in Section 31.3.3). Furthermore, the depth of the light sheet has to be chosen in such a way that the seeding particles stay long enough in the illuminated area to enable the tracking. This kind of illumination is only useful if there is a main flow direction and the light sheet is aligned in this direction.

31.2.2 Setup for stereo particle-tracking velocimetry

Flow dynamics in liquids is one of the areas in which spatiotemporal aspects govern the physical properties of the system. Following a tracer—such as seeding particles—over a sequence of images in the three dimensional space of observation yields the complete physical spatiotemporal information. From this the flow field pattern in space and time can then be reconstructed. As compared to the PIV method (see Grant [4]) where vector fields are resolved only for one time interval from a pair of images, the tracking of particles results in the flow field during a larger time span in Lagrangian coordinates.

Stereo PTV extends the classical, 2-D PTV methods to three dimensions. Therefore, the illumination should not be restricted to a light sheet but must fill an entire measuring volume. Typical setups for PTV and stereo PTV applications are presented in the next section.

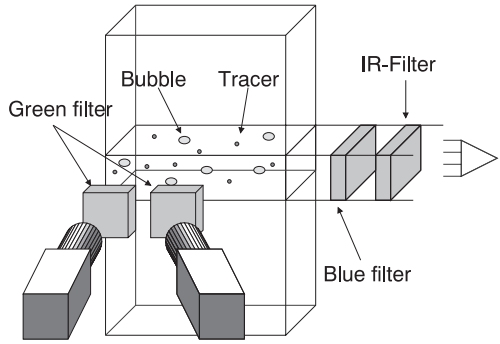

Figure 31.2: *Scheme of the water-filled bubble column and visualization for stereo PTV of the flow of water around bubbles with fluorescent tracer particles.*

31.2.3 Applications for stereo particle-tracking velocimetry

Generally, PTV methods are applied in applications where dynamic processes are investigated. Sample applications in a gas-liquid reactor and in a wind-wave flume are shown in the next two sections.

Example 31.1: The gas-liquid reactor

In the chemical industry, many process operations depend on complex multi-phase flow processes. A setup for the measurement of the water flow around the bubbles in a gas-liquid reactor is show in Fig. 31.2. Air bubbles move from the bottom to the top. The flow field of the liquid is visualized by fluorescent seeding particles (90 μm diameter) as tracers. The wavelength shift between the blue light exciting the fluorescence and the green fluorescent light makes it possible to suppress the light directly reflected from the bubbles with an appropriate colored glass filter. The motion of the bubbles can be measured with a second setup (not shown in Fig. 31.2) using a blue filter that passes only the blue light of the light source.

Example 31.2: 2-D flow visualization in a wind-wave flume

Another sample application of PTV is the study of the water flow close to the air/water interface in a wind-wave flume. The Heidelberg wind-wave flume has an annular shape. As shown in Fig. 31.3, the wind is produced by paddles driven by a belt. Due to the wind-induced momentum and the annular shape of the flume, a great average speed in the direction of wind is induced upon the water. This average speed can be compensated for by a moving bed, installed at the bottom of the flume and rotating in the opposite direction of the main flow.

A typical experimental setup for 2-D flow visualization in this facility is shown in Fig. 31.4. Due to their movement during the exposure time, the particles are imaged as streaks (Fig. 31.1). In order to track the particles over an extended period of time, the standard thin laser illumination sheets for particle-imaging velocimetry are not suitable even

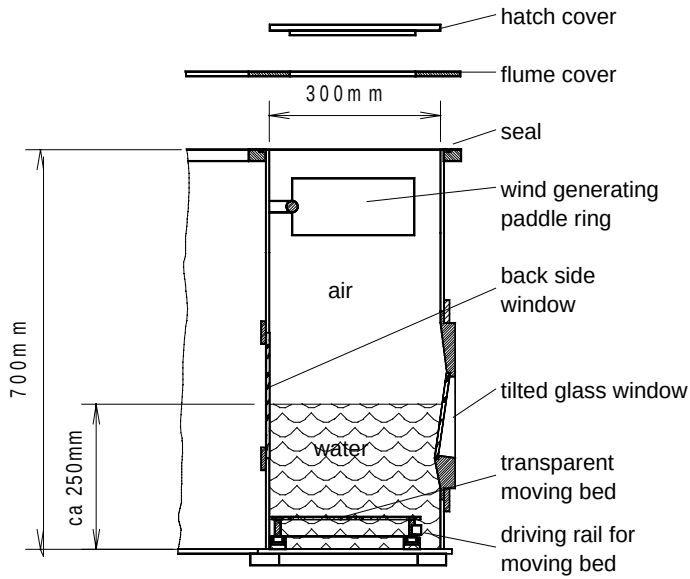

Figure 31.3: *Scheme of the cross section of the circular Heidelberg wind-wave flume.*

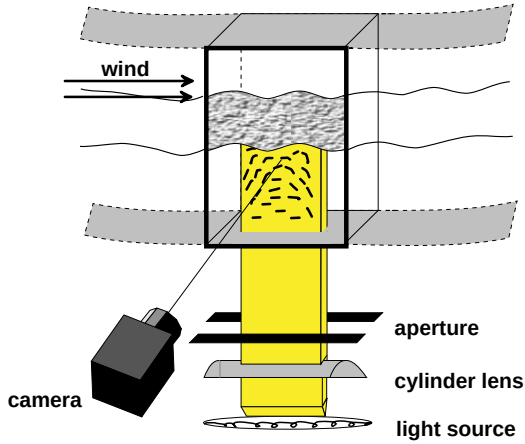

Figure 31.4: *Scheme of the experimental setup for 2-D PTV.*

if the light sheet is aligned with the main flow direction. Therefore, a halogen light source with a cylinder lens and an adjustable aperture to control the width of the illumination sheet is used. This illumination setup is also suitable for 3-D particle tracking with stereo imaging (see Netzsch and Jähne [9]) using a setup similar to that shown in Fig. 31.2.

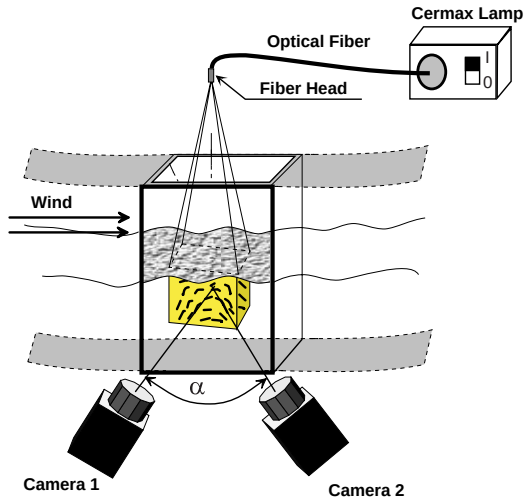

Figure 31.5: *Scheme of the experimental setup for volumetric 3-D PTV with forward scattering.*

Example 31.3: Volumetric flow visualization in a wind-wave flume

An alternative illumination setup for 3-D PTV is shown in Fig. 31.5. Here, a light source with an optical fiber is mounted on the top of the flume, opposite to the CCD cameras. This setup has two advantages over the sheet illumination techniques as discussed in Example 31.2. First, a whole volume can be illuminated. Second, it has a much lower scattering angle than the setups in Figs. 31.2 and 31.4. While the scattering angle is about 90 degrees in these setups, forward scattered light with a scattering angle between 20 degrees and 40 degrees is observed with the setup in Fig. 31.5, resulting in much brighter particle images (see Section 31.2.4).

A problem with this setup is the oblique view of the cameras through the bottom of the facility. This results in a significant lateral *chromatic aberration* (Volume 1, Section 4.5.6). Thus the bandwidth of the polychromatic xenon illumination source has to be reduced by using a red color filter. The observation volume results from the geometry of the two intersecting volumes of the two cameras. The intersecting volume (as a function of angle α) is therefore smaller than that covered by a single camera. In the setup shown in Fig. 31.5 it is about $5\,\text{cm} \times 5\,\text{cm} \times 3\,\text{cm}$.

31.2.4 Choice of seeding particles and scattering angle

Measurements of flow fields in a transparent medium such as water or air require tracers in order to represent the fluid motion correctly [10]. The ideal particle should have two properties. It should follow the flow

of the fluid without any slip and delay and it should scatter as much light as possible into the observation direction. Thus it is necessary to investigate both the flow around the particles and the scattering characteristics.

The flow-following properties of a particle depend on its size and density. Assuming spherical particles and neglecting the interaction between individual particles, the vertical flow induced by buoyancy flow can be derived and results in

$$\boldsymbol{v}_d = \frac{(\varrho_p - \varrho_f) d_p^2}{18\mu} \boldsymbol{g} \tag{31.3}$$

where d_p is the particles' diameter, μ is the dynamic viscosity, and $\boldsymbol{g}$ is the gravitational constant. The vertical drift velocity depends on the difference of the densities of fluid (ϱ_f) and tracer (ϱ_p). In order to minimize this vertical drift, the particles density should be equal to the density of the medium. While this can be achieved quite easily for flow in liquids, it is hardly possible for flow in gases.

A general equation of motion for small, spherical particles was first introduced by Basset, Boussinesq and Ossen; see Hinze [11] for details. Analysis of this equation shows how particles behave in a fluctuating flow field at frequency ω; the error $\epsilon_f(\omega)$ is then given by

$$\epsilon_f(\omega) = \text{const.}\, \omega^2 d_p^4 \tag{31.4}$$

For the evaluation of the proportionality constant see Hinze [11]. This error can be reduced by choosing small particles for the flow visualization, but because the visibility of particles is proportional to d_p^2, larger particles are better suited for flow visualization.

Wierzimok and Jähne [12] examined various particles for application in tracking turbulent flow beneath wind-induced water waves. The authors found LATEX-polystyrol particles to be suitable for this purpose. These particles are cheap and have a density of 1.047 g/cm^3. For particle diameters between 50 to 150μm, the drift speed velocity ranges from 2.5×10^{-3} to 0.6 mm/s and the error $\epsilon_f(\omega)$ is below 0.07%.

Polychromatic light scattering by tracer particles. There are three major aspects which have to be considered:

1. The light source;
2. the angle of observation relative to the light source (scattering angle);
3. and the type of tracer particles.

For PTV the seeding particles are illuminated either by a coherent monochromatic laser sheet or an incoherent polychromatic light source. The wavelength range of such a light source is often reduced

by an optical bandpass filter. It is obvious that the scattering properties of particles is influenced both by the coherency and the bandwidth of the light source. These effects are taken into account by the scattering theory. Comparison between the experimental data and the theoretical intensity distributions agree well with Mie's scattering theory. Here we only report the main results. For more details see Hering et al. [13, 14].

Different types of frequently used seeding particles were investigated such as polystyrol, hollow glass spheres, and polycrystalline material. For all investigated types it was discovered that the use of polychromatic light has a strong influence on the curve form. Whereas the intensity distribution of monochromatic light varies strongly with the wavelength, the curve for polychromatic light shows a smooth behavior around a scattering angle of 90°. The averaged distribution varies slightly whereas the fractions of high frequencies are reduced almost completely. This is in accordance with the theoretical calculated values (see Hering et al. [13, 14]).

The investigated seeding particles show an almost constant and smooth scattering intensity of polychromatic light in a certain range of the scattering angle around 90°. For polystyrol seeding particles (30 to 200 μm in diameter) the range is from 55 to 140°, for hollow glass spheres (about 35 μm in diameter) from 80 to 125° and for polycrystalline material (about 30 μm in diameter) from 80 to 150°.

The hollow glass spheres show a greater increase in scattering intensity for angles greater than 125° (up to a factor of three) than the polystyrol and polycrystal particles. A great variation of scattering intensity for all types shows for angles smaller than the region of almost constant scattering intensity.

If small seeding particles are required, a maximum of scattering intensity is desired. The largest scattering intensity is acquired in forward scattering, with an angle less than 55° in the case of the polystyrol seeding particles and also for hollow glass spheres and polychrystalline particles less than 80 μm. Although in this range the variation of intensity is large, this is the recommended scattering angle to gain a maximum of light intensity in the CCD camera sensors. Continuity of optical flow of the gray values does not exist due to the great variation of the scattering angle and therefore can not be taken into account by the PTV algorithm and the correspondence search (see Section 31.3.3).

31.3 Image processing for particle-tracking velocimetry

Several steps of image processing are required for the extraction of the flow field from the image sequences. First the particles must be segmented from the background. This is one of the most critical steps. The better the *segmentation* works, the more dense particle images

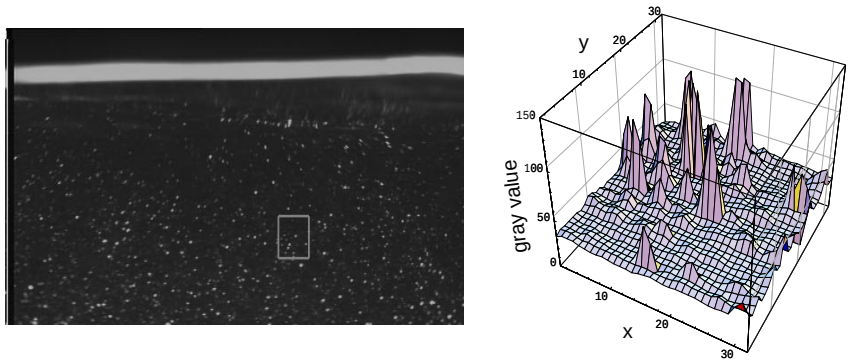

Figure 31.6: *Pseudo 3-D plot of marked area. Streaks can clearly be identified as local maxima in the gray-value distribution.*

can be evaluated resulting in denser flow fields. In this section two different segmentation algorithms are discussed: region-growing (Section 31.3.1) and model-based segmentation (Section 31.3.2). The basic algorithms for tracking segmented particles are discussed in Section 31.3.3, while the removal of bad vectors from the flow field and the accuracy of the algorithms are the topics of Sections 31.3.4 and 31.3.5, respectively. Finally, Section 31.3.6 deals with algorithms that combine the advantages of PTV and PIV.

31.3.1 Segmentation: region-growing

The intensities (gray values) of the streak images show a great variation from very low to very high values. Simple pixel-based segmentation techniques cannot be chosen since the streak images do not exhibit a true bimodal distribution in the gray-value histogram. A 'region-growing' algorithm was developed in order to discriminate individual particles from the background. Regions with similar features are identified and merged to a "connected object."

The image $g(x, y)$ is scanned for local maxima in the intensity, since the location of streaks is well approximated by a local maximum $g_{\max}(x, y)$ (Fig. 31.6). A minimum search horizontally and vertically from $g_{\max}(x, y)$ enables the calculation of the peak height

$$\Delta g = \min(g_{\max} - g_{\min}) \tag{31.5}$$

where $g_{\min}$ are the minima as revealed by a minimum search. In addition, the half-width is measured. Both peak height and half-width are

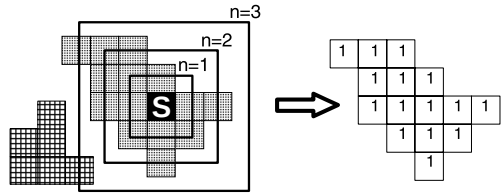

Figure 31.7: *The "region growing algorithm" will grow around the seeding point* ***s*** *until no further object points are detected.*

required to keep seeding points above a threshold. In this way random noise is not mistaken as seeding points for the region-growing algorithm.

With the seeding points identified, the region-growing algorithm segments the object (Fig. 31.7) according to the following two rules:

- a pixel to be accepted as an object point requires a gray value higher than an adaptive threshold. This is calculated by interpolation from $g_{\min}$. For details regarding computation of the threshold, see Hering [15]; and
- only pixels which form a connected object are considered.

An example result of the described segmentation algorithm is shown in Fig. 31.8. Each object identified by the segmentation is labeled with a flood-fill algorithm borrowed from computer graphics. The size of each object can then be determined, and as a result large objects (reflections at the water surface) can be removed.

31.3.2 Segmentation: model-based

The previously described region-growing algorithm yields good results as long as the particles have an approximately spherical shape. In this case a plain local maximum describes their center. However, with increasing velocity the particles are imaged as *streaks* because of their motion during exposure time. The central peak is blurred and can no longer be reliably used as a seeding point for region growing since the algorithm tends to break one streak into several smaller ones. An appropriate algorithm therefore has to take into consideration the knowledge of the streak structure.

Modeling the gray-value distribution of a streak. As shown in Hering et al. [14] the light distribution (the gray-value distribution $g_\sigma(\boldsymbol{x})$,

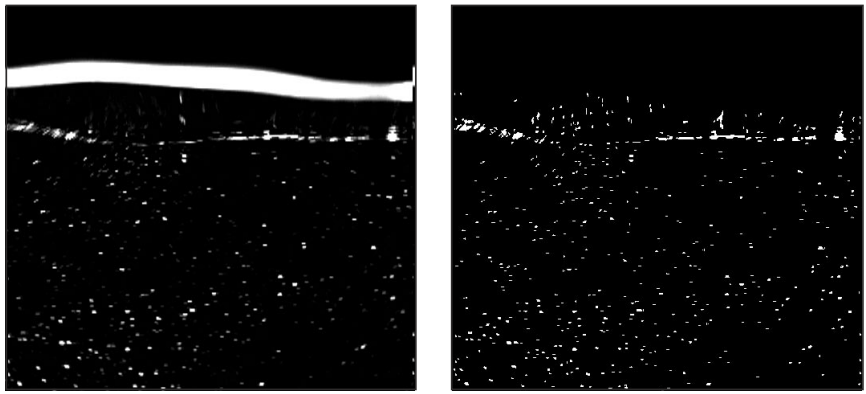

Figure 31.8: *Original gray-value image left and segmented image right. The white line on the top of the left image is due to reflections at the water surface and is eliminated by the labeling algorithm on the right image.*

respectively) of a still particle can be approximated by a Gauss function which depends only on the distance to its center of mass $\boldsymbol{\mu}$

$$g_\sigma(\boldsymbol{x}) = g_\sigma(|\boldsymbol{x}-\boldsymbol{\mu}|) \text{ with } \boldsymbol{\mu} = \frac{\int \boldsymbol{x} g_\sigma(\boldsymbol{x}) d^2x}{\int g_\sigma(\boldsymbol{x}) d^2x} \tag{31.6}$$

with σ denoting the distribution half-width. To take into account the motion during the exposure time T (assuming a constant velocity $\boldsymbol{v}$), Eq. (31.6) has to be integrated over time and thus the equivalent term for the streak distribution $g_s(\boldsymbol{x})$ is obtained

$$g_s(\boldsymbol{x}) = \frac{1}{T}\int_0^T G_\sigma^{(2)}(\boldsymbol{x}-\boldsymbol{v}t)dt \tag{31.7}$$

with $G_\sigma^{(n)}(\boldsymbol{x}) = 1/(\sqrt{2\pi}\sigma)^n \exp\left(-\boldsymbol{x}^2/2\sigma^2\right)$ representing the n-dimensional Gauss function. With the abbreviation $G(x) = G_\sigma^{(1)}(x)$ for $\sigma = 1$, Eq. (31.7) is found to be equivalent to (for an explicit calculation, see Leue et al. [16])

$$g_s(\boldsymbol{x}') = A\frac{G(\frac{1}{\sigma}|\boldsymbol{x}'\times\boldsymbol{n}|)}{l\sigma}\int_{\frac{1}{\sigma}(\boldsymbol{x}'\boldsymbol{n}-\frac{l}{2})}^{\frac{1}{\sigma}(\boldsymbol{x}'\boldsymbol{n}+\frac{l}{2})} G(\tau)d\tau \tag{31.8}$$

where $\boldsymbol{x}'$ denotes the spatial coordinate relative to the center of mass $\boldsymbol{x}' = \boldsymbol{x}-\boldsymbol{\mu}$; $\boldsymbol{n}$ is a normalized vector pointing in the particle direction of motion $\boldsymbol{n} = \boldsymbol{v}/|\boldsymbol{v}|$,and l is the length of the streak that is the distance the particle moved during exposure time. The normalization has been chosen in such a way that the parameter A describes the total sum

of the gray value. The width of the streak—normal to its direction of motion—is identical to the width σ of the still particle.

The goal is to determine these parameters with sub-pixel accuracy. This can be done by applying a least square fit of the function Eq. (31.8) to the image data. First, an area of interest is selected by the subsequent preprocessing algorithm. For this area the parameters are estimated and improved iteratively.

Preprocessing. The streaks in the image sequences are characterized by a nearly constant gray value in the direction of motion, whereas they vary rapidly in the perpendicular direction. In order to find an area that contains a streak an algorithm that emphasizes such structures is needed.

Image processing provides us with an appropriate procedure called *local orientation* (for detailed reading on this subject, see Jähne [17] and Volume 2, Chapter 10). By simply applying linear filter operations and point-wise multiplication the following three characteristics of an image can be computed for each pixel:

- the **orientation angle** lies in the range of 0 to 180° and specifies the angle that an ideally oriented structure of parallel lines would enclose with the x-axis. The fact that the angle is limited to an interval of 180° shows that it is only possible to determine the orientation of a structure but not the direction;
- the **amplitude** gives a measure for the certainty of the orientation angle; and
- with the **coherence measure** the *strength* of the orientation can be described. For an isotropic gray-value distribution this measure is zero; for an ideally oriented structure it is one.

To find regions in the image data which contain 'streaks' the coherence measure is the most effective one. It intensifies oriented structures that will be identified as streaks. Moreover, it turns out to be almost independent of the gray-value amplitudes of the streaks.

Segmentation. After calculating the coherence measure the image is binarized using a threshold. Because of the independence on the gray-value amplitude of this measure more than 90 % of the streaks can be detected even though their intensities differ widely (see Fig. 31.9) within the image.

To determine the exact streak parameters (center of mass, length, half-width, orientation, and gray-value sum) Eq. (31.8) is fitted to each binarized region by using the Levenberg-Marquardt algorithm for nonlinear regression problems [18]. Start parameters are found by calculating the region moments (see Jähne [17]). Figure 31.10 shows an example result of the model-based segmentation algorithm.

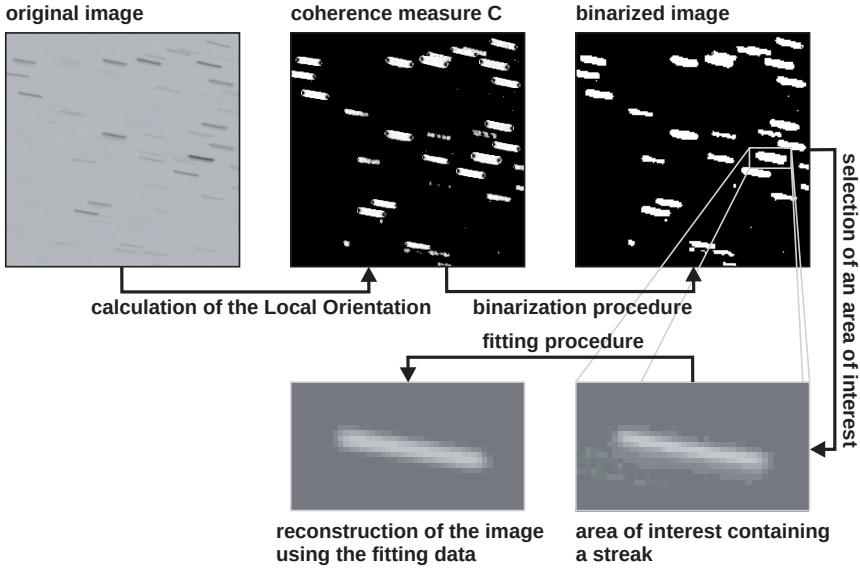

Figure 31.9: *Segmentation procedure as described in the text. On the original image the coherence measure of the local orientation is calculated and then used as an input for the binarization procedure. In a subsequent step the parameters are determined by fitting Eq. (31.8) to the image data.*

31.3.3 Image-sequence analysis

After segmentation, the *correspondence problem* of identifying the same particle in the next image frame is solved. Standard video cameras operate in a so-called *interlaced-scanning* mode (see Volume 1, Section 7.7.1). One frame is composed of two fields—one with the even, the other with the odd lines that are exposed in sequence. Thus with moving objects two different images are actually obtained with half the vertical resolution. In interlace mode, there can be an overlap in the exposure time of the two fields when each field is exposed for the full frame time (so-called frame integration mode). The overlap in the exposure time yields a spatial overlap of the two corresponding streaks from one image to the next (as illustrated in Fig. 31.11) that makes it easy to solve the correspondence problem.

However, the interlaced mode with only half the vertical resolution presents a disadvantage for particle tracking. Thus it is more useful to use modern *progressive-scanning* cameras with full vertical resolution (Volume 1, Section 7.7.3). Then corresponding particles will no longer overlap. This expansion can be increased by the use of a morphological *dilation* operator (see Wierzimok and Hering [19] and Volume 2, Sec-

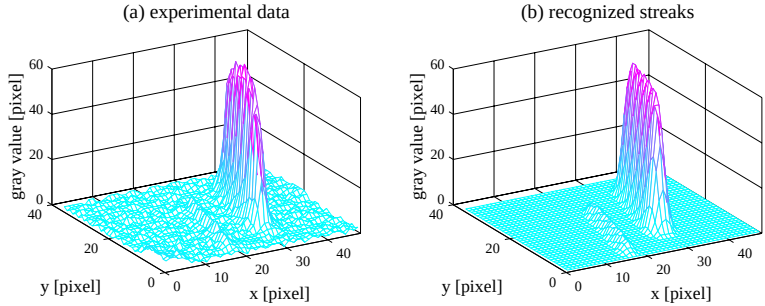

Figure 31.10: *Comparison between the experimental data and the gray-value distribution according to Eq. (31.8):* ***a*** *pseudo 3-D plot of the original data containing streaks of different intensities;* ***b*** *reconstruction of the streaks by the described algorithm. The detection of the two streaks was only possible because the coherence measure is widely independent of the gray-value amplitude.*

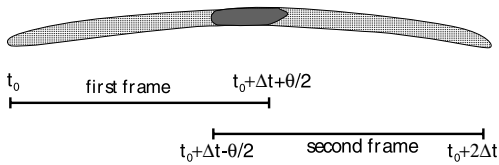

Figure 31.11: *The temporal overlap of the exposure time in two consecutive fields of the same frame yields a spatial overlap of corresponding streaks. A similar effect for images which do not overlap in time is obtained for streaks increased by the use of a morphological dilation operator.*

tion 21.3.1). This operation will enlarge objects and typically smooth their borders (see Jähne [17].) The correspondence is now found by an AND operation between two consecutive segmented fields. This correspondence of streak overlap can be calculated quickly and efficiently (see Hering [15]). In addition, because the temporal order of the image fields is known, the direction of the vector is also known and no directional ambiguity has to be taken into account.

To avoid unnecessary clustering of the objects the dilation is not calculated simultaneously for all objects in an image but for each object individually (see Hering et al. [20]). In most cases, in particular for low particle concentration ($\leq$ 300 particles/image), each particle shows only the overlap with a corresponding particle in the next frame. However, at higher particle concentration, particles show overlap with typically up to four particles in the next frame. Therefore, additional features are required to minimize false correspondences. Ideally, the sum of gray values for each streak S in the image series should roughly be

constant due to the equation of continuity for gray values (see Hering [15]):

$$\sum_{x,y \in S} g(x,y) = \text{const} \tag{31.9}$$

This implies that a particle at low speed is visualized as a small bright spot. The same particle at higher speed is imaged as a fainter object extending over a larger area. The sum of gray values in both cases should be identical. The computation of the sum of gray values, however, is error-prone due to segmentation errors which are always present. Therefore, it is more convenient to normalize the sum of gray values by the occupied area. The normalized sum of gray values being G_n^1 of the first frame and G_n^2 of the second are required to lie above a threshold of the confidence interval C

$$C \quad = \quad 1 - \frac{|G_n^1 - G_n^2|}{|G_n^1 + G_n^2|} \quad \longmapsto \quad [0,1] \tag{31.10}$$

A similar expression can be derived for the area of the objects.

Calculation of the displacement vector field. Wierzimok and Hering [19] showed that the center of gray value $\boldsymbol{x}_c$ of an isotropic object represents the time-averaged 2-D location $\langle \boldsymbol{x} \rangle_{\Delta t}$. Thus

$$\boldsymbol{x}_c = \langle \boldsymbol{x} \rangle_{\Delta t} \tag{31.11}$$

where $\boldsymbol{x}_c$ is calculated from the sum of all n segmented pixels of a streak

$$\boldsymbol{x}_c = \left(\frac{\sum_{i=1}^{n} x_i g(x_i, y_i)}{\sum_{i=1}^{n} g(x_i, y_i)} \quad , \quad \frac{\sum_{i=1}^{n} y_i g(x_i, y_i)}{\sum_{i=1}^{n} g(x_i, y_i)} \right) \tag{31.12}$$

The knowledge of the location of the same particle in the previous frame (at the time $t - \Delta t$) allows it to apply the first-order approximation of the velocity field $\boldsymbol{u}(t)$

$$\boldsymbol{u}(t) \approx \frac{\boldsymbol{x}_c(t) - \boldsymbol{x}_c(t-1)}{\Delta t} \tag{31.13}$$

Repeating the described algorithm will automatically track all encountered seeding particles from one frame to the next.

Concepts for minimizing false correspondences. The expected position of a particle is predicted by extrapolation from the vector field of previous time steps (see Wierzimok and Hering [19]). A χ^2-test evaluates the probability that a pair of particles matches. Minimizing χ^2 will

maximize the likelihood function. This technique is especially helpful when more than one overlap is encountered. By this method the most unlikely correspondences can be eliminated immediately. Using $\boldsymbol{x}_c(t)$ as a measure for the particle's average position in an image, the motion of the particle center from image to image is a discrete time series described by a Lagrangian motion; f represents the particle trajectory, with its initial location at $t = 0$. Therefore

$$\boldsymbol{x}_c(t) = f(\boldsymbol{x}_c(0), t) \tag{31.14}$$

The function f is usually not known *a priori* and in most flow conditions can only be approximated by a piecewise-algebraic function for a short period of motion. Depending on the degree of freedom n of $f^{(n)}$, it requires n previous images in order to estimate the particle location in the subsequent one. The expected position of the streak centers $\boldsymbol{x}_e(t)$ is thus estimated by

$$\boldsymbol{x}_e(t) \approx f^{(n)}(\boldsymbol{x}_c(t), ..., \boldsymbol{x}_c(t - n + 1)) \tag{31.15}$$

Two simple functions f have been implemented to predict the particle position (see also Wierzimok and Hering [19] for details). The first one ($n = 1$) assumes a constant particle velocity; the second one ($n = 2$) takes into account a constant acceleration. This can be written as a convolution (denoted by the $*$ in the following equations) with the kernel h working separately for each component of $\boldsymbol{x}_c(t)$

$$f^{(1)} = h^{(1)} * \boldsymbol{x}_c \quad \text{with} \quad h^{(1)} = [2, -1] \tag{31.16}$$

$$f^{(2)} = h^{(2)} * \boldsymbol{x}_c \quad \text{with} \quad h^{(2)} = [5, -4, 1] \tag{31.17}$$

Now the expected position $\boldsymbol{x}_e(t)$ can be compared to the calculated position $\boldsymbol{x}_c(t)$ and hence multiple correspondences can be reduced to only one.

For further optimization a fuzzy logic approach similar to that of Etoh and Takehara [21] has been chosen to maximize the possibility of finding the same particle in the next frame.

31.3.4 Removing bad vectors from the flow field

In addition to avoiding *multiple correspondences*, false or stray vectors are eliminated by a grid-interpolation technique. Note that the technique described in the following is often used for interpolation of PTV data onto a regular grid (see Agüí and Jiménez [22]). Although this technique seems to be rather crude, only minor enhancements are being made by more elaborated techniques, such as a 2-D thin spline interpolation (STS) described by Spedding and Rignot [23]. Adaptive

Gaussian windowing (AGW) is simple convolution of the vector field with a Gaussian kernel, yielding the interpolated vector field $\boldsymbol{u}_i(\boldsymbol{x}_i)$

$$\boldsymbol{u}_i(\boldsymbol{x}_i) = \frac{\sum_{j=1}^{n} \boldsymbol{u}_j(\boldsymbol{x}_j)\, \exp(-\frac{\|\boldsymbol{x}_i - \boldsymbol{x}_j\|)}{\sigma^2})}{\sum_{j=1}^{n} \exp(-\frac{\|\boldsymbol{x}_i - \boldsymbol{x}_j\|}{\sigma^2})} \tag{31.18}$$

where σ is the $1/e$–width of the convolution window. Agüí and Jiménez [22] found through Monte Carlo simulations that the optimal width of the window is directly proportional to the mean nearest neighbor distance δ

$$\sigma = 1.24\,\delta, \quad \text{with} \quad \delta = \sqrt{\frac{A}{\pi n}} \tag{31.19}$$

where A denotes the image area, with n segmented particles. This interpolation can be improved and speeded up considerably by localizing the AGW convolution. That means it is not summed up over all vectors as in Eq. (31.18), but only those vectors are taken into account which lie in a certain neighborhood. By choosing the $\boldsymbol{x}_i$ of Eq. (31.18) on a regular grid, the PTV vectors are interpolated to that regular grid. In addition, this interpolation technique can be used to remove stray vectors from the vector field. Each displacement vector gained by the PTV algorithm is compared to the interpolated vector at the same location, obtained by the AGW technique. Obvious false vectors are being eliminated as a consequence.

31.3.5 Accuracy of particle-tracking velocimetry

For testing the *accuracy* of the PTV algorithm, small particles were attached to a rotating disk of an LP-player (see Hering et al. [20]). The disk rotated at constant speed of 33 rpm; see Fig. 31.12. Therefore, as each vector of a trajectory has the same absolute velocity, one can calculate the one-sigma error $\sigma_{\overline{v}}$ for the determination of a displacement vector by

$$\sigma_{\overline{v}} = \sqrt{\frac{\sum_{i=1}^{N} (\overline{v_i} - ||\boldsymbol{v}_i||)^2}{N(N-1)}} \tag{31.20}$$

where $\overline{v_i}$ is the mean displacement, $||\boldsymbol{v}_i||$ is the ith displacement in the trajectory, and N is the number of displacement vectors in the trajectory. Figure 31.13 shows the standard error for displacement vectors of up to 12 pixels per frame, calculated from more than 100,000 vectors. The relative error remains always well below 3 %.

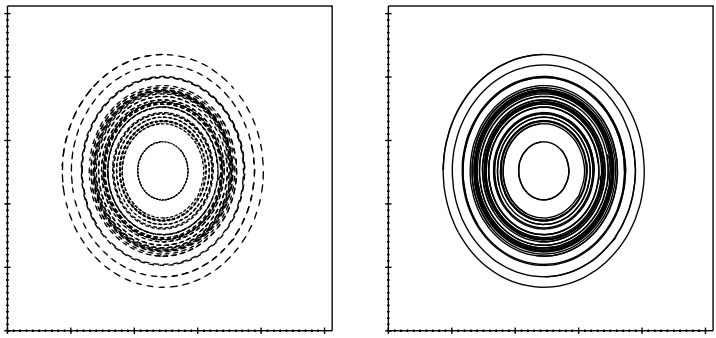

Figure 31.12: *Trajectories of particles attached to a disk rotating at 33 rpm; in the left image only every second vector is shown.*

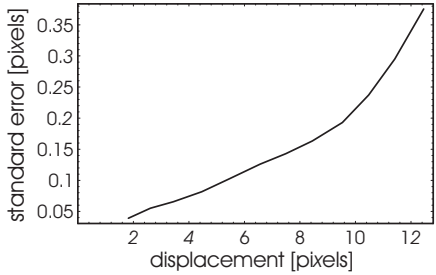

Figure 31.13: *One-sigma error for the calculation of displacement vectors.*

Multiscale particle-imaging velocimetry. The most widely used technique in modern computer-based flow visualization is based on a simple *cross correlation* of two images taken shortly after each other (PIV). A typical application records particles in a single plane within a densely seeded flow field using a pulsed laser sheet; see Fig. 31.1. The illuminated particles are imaged by a CCD sensor, taking at least two consecutive images. A sliding interrogation window of the first image $g(\boldsymbol{x})$ is matched with the second image $h(\boldsymbol{x})$ using the (unbiased) cross correlation $\Phi(\boldsymbol{s})$

$$\Phi(\boldsymbol{s}) = \frac{\sum\limits_{\boldsymbol{x}\in\epsilon} (f(\boldsymbol{x}+\boldsymbol{s}) - < f(\boldsymbol{x}) >)(g(\boldsymbol{x}) - < g(\boldsymbol{x}) >)}{\sqrt{\sum\limits_{\boldsymbol{x}\in\epsilon} (f(\boldsymbol{x}) - < f(\boldsymbol{x}) >)^2} \sqrt{\sum\limits_{\boldsymbol{x}\in\epsilon} (g(\boldsymbol{x}) - < g(\boldsymbol{x}) >)^2}} \tag{31.21}$$

This equation is effectively implemented via the 2-D fast Fourier transform (FFT) of the two image samples and a complex conjugate multiplication. Finally, the inverse transformation yields the standard

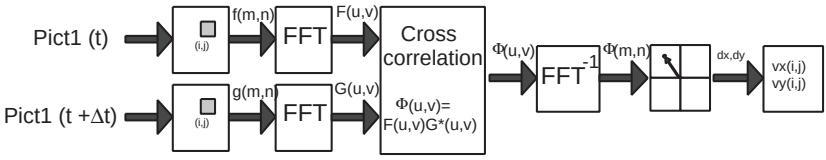

Figure 31.14: *Scheme for the calculation of the cross correlation, as used for digital imaging velocimetry.*

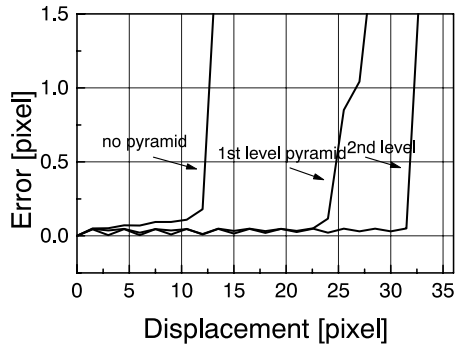

Figure 31.15: *Error of multi-scale PIV with a 32× 32 wide correlation window as a dependency of the pyramid level.*

cross correlation. With a peak-fitting routine the most likely displacement (highest correlation) is detected (see Fig. 31.14).

Various techniques for peak finding are reported in the literature (for a review, see Gharib and Willert [7]). Typical displacements correctly extracted are in the order of half the size of the correlation window ϵ (see Fig. 31.15). In order to extend this technique to larger displacements a new *multiscale* approach will be presented in this chapter that is similar to the techniques described in Volume 2, Chapter 14.

The original images are decomposed in their *Gaussian pyramids* (see Burt and Adelson [24] or Volume 2, Section 4.4.2). On each level (going from the coarse structures to the finer structures) the cross correlation is computed. These displacements are serving as a velocity estimator for the next (finer) pyramid level. This technique allows a drastic increase in the maximum length of a displacement vector, up to approximately the size of the correlation window ϵ (see Fig. 31.15).

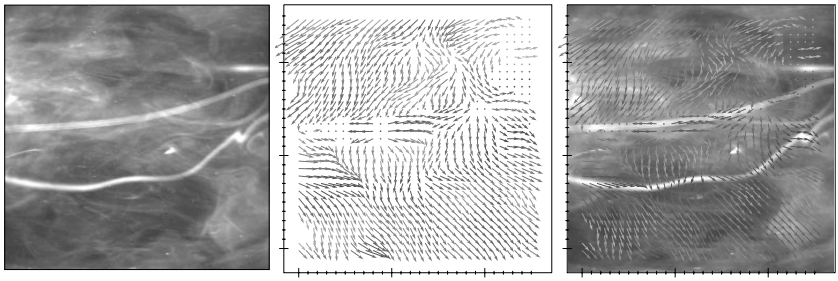

Figure 31.16: *Structure tensor: example of a laser-induced fluorescence (LIF) visualization with the computed displacement vector field.*

The structure tensor approach. Using the 3-D *structure tensor* technique, dense *displacement vector fields* (DVF) can be computed with sub-pixel accuracy on a pixel basis. The approach is based on the detection of linear symmetries and the corresponding orientation angle within a local spatiotemporal neighborhood of *space-time images*. The technique does not depend on the image content and is well suited for particles and for continuous tracers in flow visualization. Section 13.3.2 in Volume 2 gives a detailed description of this method.

This basic property of spatiotemporal images allows estimating the optical flow from a 3-D orientation analysis, searching for the direction of constant gray values in spatiotemporal images. As an example, Figure 31.16 shows the displacement vector field of an LIF image sequence computed with the structure tensor technique. It can be shown that this technique yields displacements with high sub-pixel accuracy of less than 0.01 pixels/frame. However, the maximum displacement is limited by the temporal sampling theorem and can only be extended by the multi-grid technique described in the foregoing section.

31.3.6 Hybrid particle-imaging/particle-tracking velocimetry

Because many particles are within the correlation window of the PIV technique, the resulting velocity field is of lower spatial resolution but is more reliable than the velocity estimate determined by PTV techniques for a single particle. With rather high particle concentrations a high number of correspondences are also lost. Thus it appears to be worthwhile to combine the advantages of PIV and PTV techniques into a hybrid PIV/PTV method.

The simplest approach is to use the velocity field obtained by particle image velocimetry as an initial velocity estimator for the tracking algorithm. Indeed, this combination results in several improvements. First, the length of the extracted trajectories is increased indicating

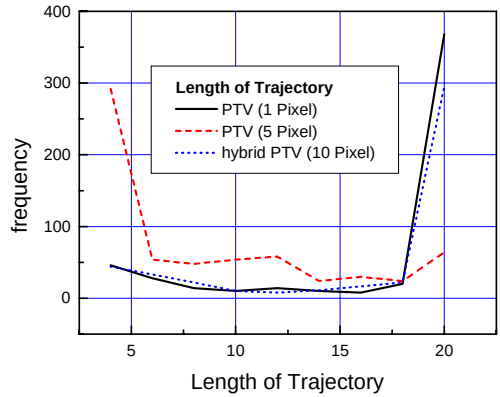

Figure 31.17: *Length of trajectories of particles attached to a rotating disk.*

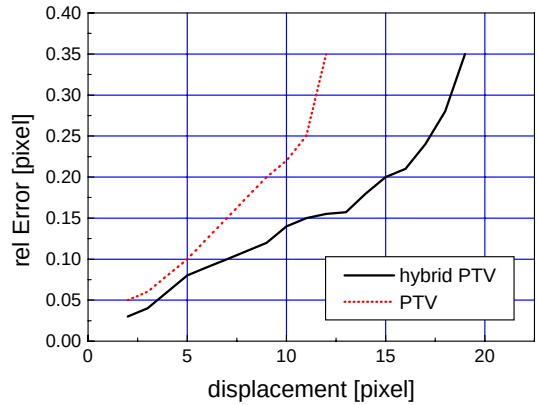

Figure 31.18: *Mean position error for hybrid PTV system.*

that a trajectory is less frequently cut off due to a missing correspondence (Fig. 31.17). Whereas without an initial velocity estimation many particles are lost, the hybrid system allows most of the particles to be tracked even at high displacements. Second, Fig. 31.18 shows that streaks can be tracked over longer image sequences. Third, the relative error in the displacement estimate is significantly reduced, especially for large displacements.

31.4 Stereo particle-tracking velocimetry

The fundamental problem of stereo PTV is the correspondence problem. The stereo correspondence problem is generally solved by comparing images taken from different camera perspectives. This approach

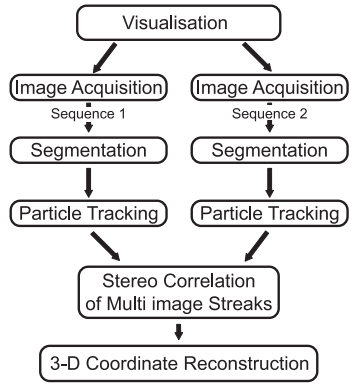

Figure 31.19: *Steps of the stereo PTV algorithm.*

presents ambiguities that become more severe with increasing particle density [25]. There are two ways to solve the correspondence problem. The first way is to solve it by capturing individual images. As shown by Maas et al. [25] this is not possible with only two cameras. The basic problem is that the particles can barely be distinguished from each other. With two cameras, corresponding particles cannot be identified in a unique way since the particle in one image can have a corresponding particle at a line across the whole field of view in the second camera (*epipolar line*, see Volume 2, Chapter 17). Thus, at least three cameras are required for a unique correspondence (two epipolar lines intersect each other in one point if the corresponding stereo bases are not parallel to each other).

The second approach [9] computes the trajectories for each of the stereo cameras first with the PTV techniques described in Section 31.3. The hope, then, is that the trajectories are sufficiently different from each other so that a unique correspondence is possible. The resulting trajectories from each camera perspective can then be matched

The main steps of this algorithm are shown in Fig. 31.19 and will be described in the following sections. The stereo calibration supplies the parameter set for the camera model (Section 31.4.1) used for the stereoscopic reconstruction. The image sequences of the two cameras are then processed separately to extract the trajectories of particles in two dimensions. Finally, the stereo correlation of the trajectories from the two cameras provide the trajectories in 3-D space. In conjunction with the parameter set of the camera model, the spatial coordinates can be obtained.

31.4.1 Geometric camera calibration

To obtain quantitative results in digital image processing the geometric camera calibration is an essential part of the measuring procedure and evaluation. Its purpose is to give a relation between the 3-D world coordinate of an object and its 2-D image coordinates. A geometric camera model describes the projection transformation of a 3-D object onto the 2-D CCD sensor of the camera. The quality of the camera calibration is crucial for the accuracy of the stereoscopic reconstruction. Effects not included in the camera model will result in a systematic error.

31.4.2 The camera model

The camera model $\boldsymbol{F}$ is the mathematical description of the relation between the 3-D world coordinates $\boldsymbol{X}$ and the 2-D image coordinates $\boldsymbol{x}$ (see Volume 1, Chapter 17):

$$\boldsymbol{x} = \boldsymbol{F}(\boldsymbol{X}) \tag{31.22}$$

The simplest model is the pinhole camera model. This model is described by four linear transformations including the ten parameters of translation $\boldsymbol{T}$ (3 offsets), rotation $\boldsymbol{M}$ (3 angles), projection $\boldsymbol{P}$ (focal point) and scaling S

$$\boldsymbol{F} = S\boldsymbol{T}\boldsymbol{M}\boldsymbol{P} \tag{31.23}$$

An extended model includes also lens distortion (compare Volume 1, Section 4.5.5 and Chapter 17). Lens distortion is described by a nonlinear correction (see Hartley [26]).

Multimedia geometry. In many applications the camera and the optical system have to be mounted outside the volume of observation. The camera looks, for example, through a glass or Perspex window into the water (see Fig. 31.20). Therefore, a multimedia correction seems to be necessary. The light is refracted according to Snellius' law. Its effect is described by a displacement from the straight line $\Delta X = X_0 - X_{mm}$. If the geometry of the setup is known, ΔX is a function of X_w and of the location of the camera X_k. As this function has no analytical solution, ΔX has to be calculated numerically applying Fermat's principle.

Parameter estimation. The nonlinearity of the camera model does not allow computing the parameters in a direct analytical way. Therefore, a nonlinear minimization method (Levenberg-Marquardt algorithm [18]) is used. The function to minimize is

$$\text{Res} = \sum_i (x_i - \mathbf{F}(X_i))^2 \tag{31.24}$$

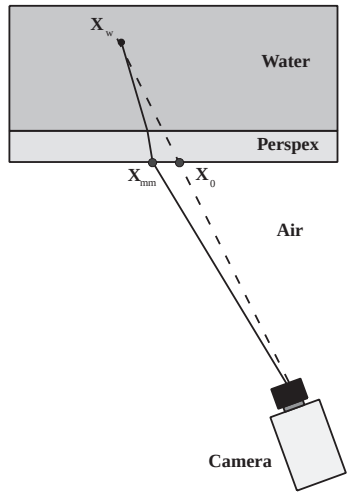

Figure 31.20: *Distortion by multimedia geometry.*

To avoid the algorithm from getting caught in a local minimum, a choice of proper initial values is critical. This can be guaranteed by neglecting the nonlinear part of the camera model (k_1, k_2, p_1, and p_2 set to zero). The parameters of the remaining linear model which are determined by a direct linear transform (DLT) (see Melen [27]), yield the initial values.

Inversion of the camera model. The camera model describes the transformation from world to image coordinates. For the evaluation the inverse relation is of interest—to obtain world coordinates of an object from its position in the 2-D image.

Because the camera model projects a point in 3-D space to a point in a 2-D plane, the solution of the inversion of the camera model is a line. The intersection of the two lines gives the 3-D position of the object (triangulation problem [26]). Mainly due to noise error the lines do not exactly intersect. Therefore, the midpoint of the minimum distance of the two lines is taken as the "intersection point." To invert the camera model a numerical method has to be used because an analytical solution does not exist. For an image point $\boldsymbol{x}$ and a given Z-coordinate Z_0 the world point $\boldsymbol{X}$ to be found is given by the minimum of

$$\epsilon = \left| \boldsymbol{x} - \mathbf{F}(\boldsymbol{X}) \right|_{Z=Z_0} \tag{31.25}$$

As this function is convex, a gradient-based minimization routine always converges.

Table 31.1: Comparison of camera models

Camera model	Residue in pixel^2
Without multimedia correction	0.121
With multimedia correction	0.325

31.4.3 Virtual camera

First, the accuracy of the camera model can be tested with and without the multimedia correction. The quality of the camera model can be quantified by the residue as defined in Eq. (31.25).

As shown in Table 31.1, the model without the multimedia correction yields lower residue and therefore a better result. Taking multimedia correction into account, the exact position of the two cameras is required. In the camera model the z coordinate of the camera and the focal length are highly correlated parameters. Therefore, the camera position is quite uncertain and the multimedia correction is not exact.

Because of the lower residue the model that does not take multimedia correction into account is better suited. Therefore the positions of the cameras are virtual. The actual world coordinates of the cameras are not necessary for the stereo reconstruction described in the following sections.

31.4.4 Stereoscopic correspondence

Using a calibrated stereo rig the 3-D trajectories can be reconstructed from the 2-D trajectories by solving the stereoscopic correspondence problem. In order to reconstruct the location of the trajectory in 3-D space, its image coordinates (x, y) and (x', y') for both cameras have to be found. This will be described in detail in the following sections. A general discussion on the geometry of stereo imaging and the determination of the stereo disparity can be found in Volume 2, Chapters 17 and 18, respectively. From (x, y) and (x', y') it is possible to perform the triangulation with the knowledge gained by the calibration procedure discussed in Section 31.4.1.

The epipolar constraint. The computational efficiency of establishing stereoscopic correspondences is increased by introducing the *epipolar constraint*. It is derived from stereoscopic geometry and as such is a very strong constraint. As stated in Section 31.4.2, the object has to be located on the outgoing ray of the first camera as can be seen in Fig. 31.21. This ray is in turn depicted by the second camera as the so-called *epipolar line*. The endpoints of the epipolar line are called

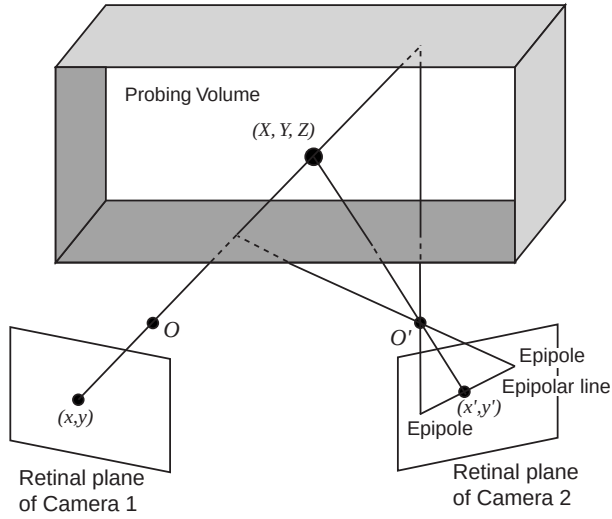

Figure 31.21: *Construction of the epipolar line in the retinal plane of camera 2 from an image point (x, y) on the retinal plane of camera 1.*

epipoles. They are defined by the finite depth range of the probing volume. This constraint is, of course, symmetric for both cameras.

Due to noise and a small error in determining the camera parameters a certain tolerance ϵ is added to the epipolar line. It will thus be a narrow window in image space as is shown in Fig. 31.22.

Taking lens distortion and multimedia geometry into account, the epipolar line will deviate from a straight line and be slightly bent. In practice this curvature proved to be small enough to be accounted for by the tolerance ϵ. For practical purposes the epipolar line is thus replaced by an epipolar window.

31.4.5 The stereo correlation algorithm

In a first step a list of possibly corresponding candidates is constructed. The candidates obey two constraints:

- the time constraint: corresponding trajectories were tracked at the same time; and
- the *epipolar constraint*: the corresponding trajectory T_2 to trajectory T_1 was found within the epipolar window.

Depending on particle densities these two constraints may suffice to allow a unique solution of the correspondence problem. This may not always be the case as high particle densities are beneficial for high

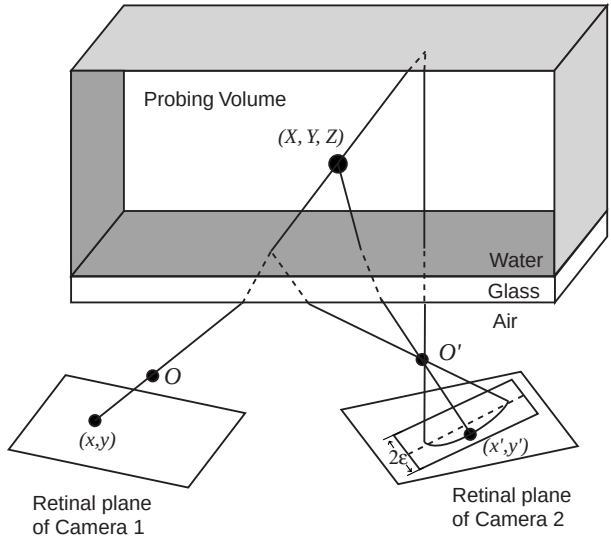

Figure 31.22: *The epipolar line for a multimedia setup. The tolerance ϵ is added to compensate for noise and the curvature.*

spatial resolutions in visualizing flows.

Generally, there are four possible outcomes of the correspondence search (see Fig. 31.23):

(1) *no correspondence:* To a trajectory T_1 in the first camera no corresponding trajectory T_2 was found in the second image;

(2) *one-to-one correspondence:* Exactly one corresponding trajectory T_2 was found for a trajectory T_1;

(3) *one-to-many correspondence:* For a trajectory T_1 multiple trajectories $T_{2,i}$ were found, which, in turn all correspond to the same trajectory T_1; and

(4) *many-to-many correspondence:* Multiple trajectories $T_{2,i}$ were found for a trajectory T_1, whereby $T_{2,i}$ also corresponds to different trajectories $T_{1,i}$.

In case (1) there exist no corresponding pairs of trajectories for which the triangulation could be performed, thus no world coordinates (X, Y, Z) can be computed. This occurs when a particle is imaged by only one camera. To avoid this it is important to maximize the overlap of the two camera footprints. Another reason might be that streaks are not segmented and tracked correctly. As a countermeasure the illumi-

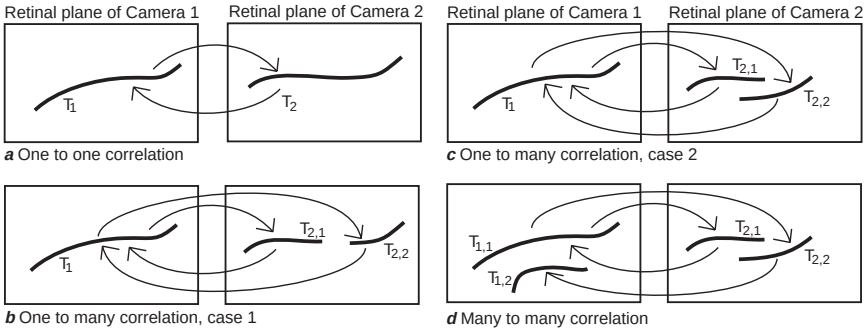

Figure 31.23: *Some possible cases that may occur during correspondence search.*

nation should be homogeneous over the whole visible volume of both cameras.

For case (2) the correlation was established and the world coordinates (X, Y, Z) of the trajectory can readily be calculated.

There are two distinct possibilities for case (3) to occur. The first is that the trajectories $T_{2,i}$ do not overlap in the time domain. This may be the case when a streak in the second camera was not segmented correctly over the whole time interval of the trajectory T_1. The resulting trajectories $T_{2,i}$ are thus generated by the same particle and can be marked as corresponding to T_1.

Case (3) occurs if the trajectories $T_{2,i}$ overlap at the same point in time. Clearly, this violates the boundary condition that trajectories have to be unique. The trajectories $T_{2,i}$ must thus belong to different particles. New criteria have to be found to overcome these ambiguities. This possibility is thus akin to case (4), where multiple trajectories $T_{2,i}$ were found for a trajectory T_1, all of which correspond to different trajectories $T_{1,i}$.

Criteria for resolving ambiguities. A strong constraint in solving the remaining ambiguities is the uniqueness constraint. This constraint states that an object point projected onto the first image should match at most with just one image point in the other view. This constraint does not hold for transparent objects over a certain size such as bubbles, where reflections may result in a single image point in one view and in two image points in the other.

For flow visualization the use of a symmetric setup with respect to illumination of small particles that are rotationally symmetric is of advantage. The particles may thus be viewed as point objects to which the uniqueness constraint may be applied.

For experiments at the bubble column—where the diameter of the bubbles is typically up to 0.5 cm—it is, of course, desirable to make use of this constraint as well. This is achieved by positioning the two cameras in such a way that their retinal planes enclose a small angle of 20° to 30° only. The bubble can then be viewed as a single point in space.

The trajectories are constructed from individually segmented streaks S_i. Invalid segmentation may therefore lead to limitations of the uniqueness constraint as not all streaks $S_{1,i}$ in the first image correlate to streaks $S_{2,j}$ in the second image. This is accounted for by a heuristic threshold value K that is determined by the number of correlated streaks k of the trajectories to noncorrelated streaks n, or $K = k/n$. If the trajectory T_1 comprises i streaks $S_{1,i}$ and the trajectory T_2 comprises j streaks $S_{2,j}$, then the number of correlated streaks k is given by $k = \min(j, i)$ and the number of uncorrelated streaks n is given by $n = |j - i|$. Therefore the threshold K can be written as

$$K = k/n = \min(j, i)/|j - i| \tag{31.26}$$

Another possible solution to the correspondence problem is statistical in nature. We stated in the foregoing that in real-world situations correlated streaks in one image will generally not be found exactly on the epipolar line of the second image due to noise and camera distortion. Therefore, the standard deviation σ_d can be calculated for the distance d from all the streaks of correlated trajectories to the epipolar line.

If the two trajectories correspond to each other, the distance d will be due solely to the tolerance of calculating the epipolar line. It should roughly be the same for all streaks of the trajectory and accordingly the standard deviation σ_d remains small.

If the two trajectories do not correspond, then d will be proportional to the relative motion of the two tracked particles and σ_d is expected to be much greater than in the other case. This makes it possible to solve some ambiguities by thresholding σ_d.

31.4.6 Results

In Fig. 31.24 the trajectories of the uprising bubbles can be seen. On the left part of the image the bubbles move upwards in a straight motion, on the right part of the image the flow is more turbulent (see Chen et al. [28]). The sequence consists of 350 images, and about 300 3-D trajectories were extracted from about 3000 trajectories obtained by PTV.

Figure 31.25 shows the trajectories of visualized and tracked particles, representing the flow beneath a free wind-driven wavy water surface. The sequence of 500 images covers a time interval of 8.3 s. The

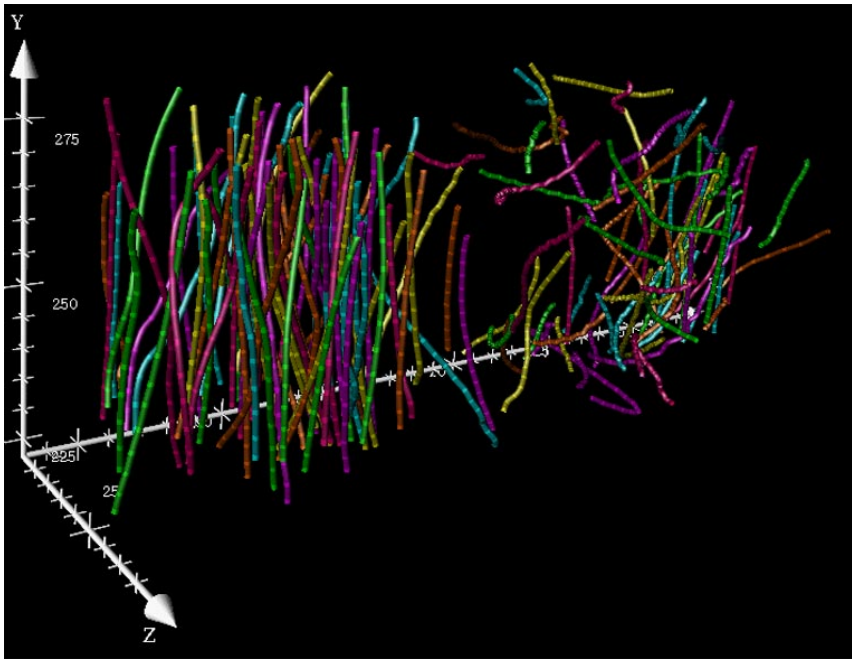

Figure 31.24: *Three-dimensional trajectories of bubbles from bubble column.*

spirally shaped trajectories result from the orbital motion of small-amplitude (< 0.5 cm) gravity waves with little steepness (< 5°).

Depending on conditions, from about 10 to 30 % of the 2-D trajectories in the stereo images, 3-D trajectories can be computed. The smaller number of 3-D trajectories compared to the 2-D trajectories is also due to geometric reduction of the intersecting volume from the two cameras. For example, if the angle α enclosed by the two cameras (Fig. 31.5) is 60° and the depth of focus is 4 cm, the maximum intersecting volume is 75 % (ideal case) of the volume observed by a single camera. The large α is chosen in favor of a higher resolution in depth (z-direction). If the light intensity is homogeneous and constant over time, the PTV can track particle or bubble trajectories over the whole sequence of images. This is well illustrated by the results gained from the bubble column in Fig. 31.2.

In the instance of flow visualization in the wind-wave flume the situation is more difficult. The number of reconstructed 3-D trajectories is much less than extracted by PTV and the length of the trajectories is shorter compared to the bubble column. Therefore, the higher density, the smaller size, and the greater velocity of the particles increase the number of ambiguities in the correlation step. If the variation of steepness is small between successive images, which is the case for

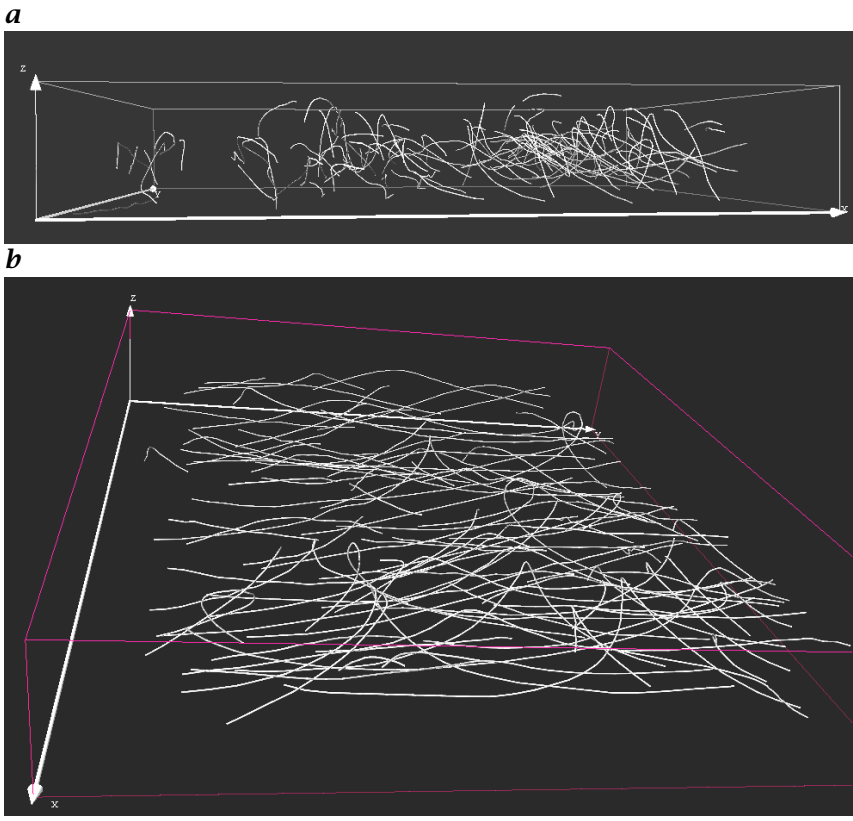

Figure 31.25: *Three-dimensional trajectories visualizing flow, two different perspectives:* ***a*** *perpendicular to the water surface and parallel to the main direction of flow;* ***b*** *perpendicular to the main direction of flow and in a slight angle onto the water surface.*

small-amplitude gravitational waves, the PTV works well to gain an insight into the 3-D flow field pattern beneath the water surface.

31.5 Conclusions

Stereo particle-tracking velocimetry is a powerful method for studying dynamic processes. For applications in flow field visualization the tracking of particles works for a concentration of up to 800 particles per image. In a 512×512 image this corresponds to a mean distance between the particles of about 30 pixels. Table 31.2 shows a comparison of the previously described flow field diagnostic techniques. For comparison all numbers given refer to an image size of 512×512 pixels.

Table 31.2: *Comparison of particle-tracking velocimetry methods*

	PIV	Hybrid PTV	Stereo PTV	Structure tensor
Tracer	discrete	discrete	discrete	continuous
Flow field	DVF	DVF *and* trajectories	trajectories	DVF
Particle Density	≈ 3000	< 1000	< 1000	–
Averaging	spatial	spatial (DFV)	no	spatial, temporal
Measure of certainty	yes	no	no	yes

Investigations of flow dynamics close to the air-water interface in a wind-wave flume and in a bubble column were shown as sample applications of stereo PTV. The method is useful for many other purposes in addition to flow visual applications. The only requirements for visualization are visible tracer objects such as seeding particles.

With stereo PTV a high spatial and temporal resolution can be obtained. Applying the calibration method described in Section 31.4.1 the spatial resolution can be sub-pixel accurate. The temporal resolution depends on the image acquisition rate of the CCD camera and on the frame grabber alone. PTV yields both the Eulerian and Lagrangian representation of the flow field, whereas PIV gives the Eulerian representation only. The Eulerian representation can be calculated from the Lagrangian representation. This clearly shows the advantage of the presented PTV methods in the study of dynamic processes. Nevertheless, the density of tracer particles in PIV methods can be greater (up to a few thousand/image) than for PTV methods. The combination of both techniques such as the hybrid PIV/PTV described in Section 31.3.6 can produce even better results.

For practical purposes an easy experimental setup is always of advantage. Therefore, the simple stereo PTV setup described in section Section 31.2.1 and Section 31.4, including only two cameras, is a useful choice to determine 3-D trajectories in a measuring volume.

Acknowledgments

Financial support for this research from the U.S. National Science Foundation through grant OCE91-15994 and the German Science Foundation (DFG) through grant Wi 1029/2-1 is gratefully acknowledged.

31.6 References

[1] Koochesfahani, M. M. and Dimotakis, P. E., (1985). Laser induced fluorescence measurements of mixed fluid concentration in a liquid shear layer. *AiAA Journ.*, **23**:1699–1707.

[2] Koochesfahani, M. M. and Dimotakis, P. E., (1986). Mixing and chemical reactions in a turbulent liquid mixing layer. *J. Fluid Mech.*, **170**:83–112.

[3] Maas, H.-G., Stefanidis, A., and Grün, A., (1994). From pixels to voxels—tracking volume elements in sequences of 3-D digital images. In *IAPRS Proc.*, Vol. 30, p. Part 3/2.

[4] Grant, I., (1997). Particle image velocimetry: a review. In *Proc. Instn. Mech. Engrs.*, Vol. 211 of *C*, pp. 55–76.

[5] Adrian, R., (1991). Particle-imaging techniques for experimental fluid mechanics. *Ann. Rev. Fluid Mech.*, **23**:261–304.

[6] Hesselink, L., (1988). Digital image processing in flow visualization. *Ann. Rev. Fluid Mech*, **20**:421–485.

[7] Gharib, M. and Willert, C., (1988). Particle tracing revisited. In *Proceedings, 1st National Fluid Dynamics Congress, Cincinnati/Ohio, AIAA-88-3776-CP*.

[8] Adamczyk, A. and Rimai, L., (1988). 2-Dimensional particle tracking velocimetry (PTV): Technique and image processing algorithm. *Experiments in Fluids*, **6**:373–380.

[9] Netzsch, T. and Jähne, B., (1995). A high performance for 3-dimensional particle tracking velocimetry in turbulent flow research using image sequences. *Proc. ISPRS Intercommission Workshop 'From Pixels to Sequences', Zurich*, **30**(5W1).

[10] Schmitt, F. and Ruck, B., (1986). Laserlichtschnittverfahren zur qualitativen Strömungsanalyse. *Laser und Optoelektronik*, **2**:107–118.

[11] Hinze, J., (1959). *Turbulence*. New York: McGraw-Hill.

[12] Wierzimok, D. and Jähne, B., (1991). Measurement of wave-induced turbulent flow structures using image sequence analysis. In *2nd Int. Symp. Gas Transfer at Water Surfaces, Minneapolis 1990*. Am. Soc. Civ. Eng.

[13] Hering, F., Leue, C., Wierzimok, D., and Jähne, B., (1997). Particle tracking velocimetry beneath water waves part I: Visualization and tracking algorithms. *Experiments in Fluids*, **23**(6):472–482.

[14] Hering, F., Leue, C., Wierzimok, D., and Jähne, B., (1998). Particle tracking velocimetry beneath water waves part II: water waves. *Experiments in Fluids*, **24**:10–16.

[15] Hering, F., (1996). *Lagrangesche Untersuchungen des Strömungsfeldes unterhalb der wellenbewegten Wasseroberfläche mittels Bildfolgenanalyse.* , Institute for Environmental Physics, University of Heidelberg.

[16] Leue, C., Hering, F., Geissler, P., and Jähne, B., (1996). Segmentierung von Partikelbildern in der Strömungsvisualisierung. In *Proc. 18. DAGM-Symposium Mustererkennung, Informatik Aktuell*, B. Springer, ed., pp. 118–129.

[17] Jähne, B., (1996). *Digital Image Processing: Concepts, Algorithms and Scientific Applications*. 2nd edition. Berlin: Springer.

[18] Press, W. H., Flannery, B. P., Teukolsky, S. A., and Vetterling, W. T., (1992). *Numerical Recipes in C: The Art of Scientific Computing*. New York: Cambridge University Press.

[19] Wierzimok, D. and Hering, F., (1993). Quantitative imaging of transport in fluids with digital particle tracking velocimetry. *Imaging in Transport Processes, Begell House*, pp. 297–308.

[20] Hering, F., Merle, M., Wierzimok, D., and Jähne, B., (1995). A robust technique for tracking particles over long image sequences. In *Proc. ISPRS Intercommission Workshop 'From Pixels to Sequences,' Zurich, In Int'l Arch. of Photog. and Rem. Sens.*, Vol. 30 of *5W1*.

[21] Etoh, T. and Takehara, K., (1992). An algorithm for tracking particles. In *Proceedings, 6th International Symposium on Stochastic Hydraulics, Tapei*.

[22] Agüí, J. and Jiménez, J., (1987). On the performance of particle tracking. *J. Fluid Mech.*, **185**:447–468.

[23] Spedding, G. and Rignot, (1990). Performance analysis of grid interpolation techniques for fluid flows. *Exp. Fluids*, **15**:417–430.

[24] Burt, P. and Adelson, E., (1983). The Laplacian pyramid as a compact image code. *IEEE Trans. COMM.*, **31**:532–540.

[25] Maas, H. G., Gruen, A., and Papantoniou, D., (1992). Particle tracking velocimetry in three-dimensional flows. Part 1: Photogrammetric determination of particle coordinates. *Exp. Fluids*, **15**:133–146.

[26] Hartley, R., (1997). Triangulation. *Computer Vision and Image Understanding*, **68**(2):146–157.

[27] Melen, T., (1994). *Geometrical Modeling and Calibration of Video Cameras for Underwater Navigation*. PhD thesis, Norges tekniske høgskole, Institutt for teknisk kybernetikk, Trondheim, Norway.

[28] Chen, R., Reese, J., and Fan, L.-S., (1994). Flow structure in a three-dimensional bubble column and three-phase fluidized bed. *AIChE J.*, **40**: 1093.